doi:10.3788/gzxb20174602.0212002

逆向工程中基于共轴立体视觉的曲面边界测量

卢科青,王文,张敏,赵春峰
(杭州电子科技大学 机械工程学院 机械电子工程研究所,杭州 310018)

摘 要:针对逆向工程中引导性曲面边界信息的快速获取问题,系统地研究了共轴立体视觉测量方法,建立该方法的数学模型,详细分析了摄像机焦距、基线距等系统结构参数及被测点空间位置对测量精度的影响,通过数学分析确定摄像机基线距的最佳取值范围,研究共轴立体视觉测量系统特殊的极线几何关系.提出基于共轴立体视觉的曲面边界快速测量方法,利用三坐标测量机的精密机械系统及精确的空间定位能力,用单个摄像机以两次共轴定位摄取图像的方式实现共轴立体视觉测量功能,然后利用共轴立体视觉外极线相互平行且通过各自像平面主点的特殊极线几何关系简化同源像点匹配过程,从而快速获取被测曲面的边界信息.实验结果表明:用基于三坐标测量机的单摄像机共轴立体视觉测量方法获取的曲面边界平均误差为 0.268 mm,基本满足逆向工程中对引导性曲面边界的测量精度要求.

关键词:立体视觉;逆向工程;边界提取;图像处理;图像匹配
中图分类号:TG806; TP391 **文献标识码**:A **文章编号**:1004-4213(2017)02-0212002-17

Digitization of Surface Boundary Based on Coaxial Stereo Vision Photogrammetry in Reverse Engineering

LU Ke-qing, WANG Wen, ZHANG Min, ZHAO Chun-feng
(*Institute of Mechatronic Engineering, College of Mechanical Engineering, Hangzhou Dianzi University, Hangzhou* 310018, *China*)

Abstract: Low-level precision boundary information of the unknown surface is useful for digital sensor path planning, data segmentation and feature recognition in reverse engineering. In order to acquire the low-level boundary information of the measured surface both rapidly and easily, the Coaxial Stereo Vision Photogrammetry (CSVP) was systematically studied. The mathematical model of CSVP was established, the influences of system parameters including the focal length of the cameras, the baseline distance and the spatial position of the measured points on measuring accuracy were analyzed, and the mathematical analysis for determining the optimum range of the baseline distance of the two cameras was carried out. In addition, the characteristics of the CSVP epipolar geometry were studied. Then a new approach for rapid digitization of surface boundaries based on CSVP was proposed. This approach was characterized by an integrated use of a Coordinate Measuring Machine (CMM) and a single CCD camera, the CMM was employed to provide an accurate and repeatable platform for the camera. Consequently, the camera can be located at any predefined position within the CMM's working volume. This enables the camera to get stereo image pairs in different positions along the same axis, which can only be achieved by two cameras without the CMM. During data processing, the characteristics of the CSVP epipolar geometry, in which the corresponding epipolar lines in the front and back image planes are arranged parallel to each other,

Foundation item: The National Natural Science Foundation of China (Nos. 51105332, 51275465), the Science and Technology Plan of Zhejiang Province (No. 2014C31096) and the Key Program of Zhejiang Provincial Natural Science Foundation of China (No. LZ16E050001)

First author: LU Ke-qing (1980-), male, lecturer, Ph. D. degree, mainly focuses on surface coordinate metrology and reverse engineering. Email:lkq@hdu.edu.cn

Received: Aug. 5, 2016; **Accepted**: Oct. 12, 2016

and the epipolar lines pass through the main points of their own image planes respectively, were applied to facilitate stereo matching, by which the surface boundary information of the measured surface can be obtained both rapidly and easily compare to conventional binocular stereo vision method. Experimental results indicate that the average error of the surface boundaries reconstructed by the data gathered by the proposed method is 0.268 mm. It can meet the accuracy requirements of low-level boundary information in reverse engineering.

Key words: Stereo vision; Reverse engineering; Boundary extraction; Image processing; Stereo matching

OCIS Codes: 120.3940; 150.0155; 150.3045; 150.6910; 010.3920; 040.1490

0 Introduction

Reverse Engineering (RE) is the process of creating a digital model from an existing physical object[1]. In reverse engineering, surface boundaries refer to the edge contours of the physical part or the edges formed by intersection of the surface patches of the physical object. Surface boundary information plays an important role throughout the RE modeling process move from 3D data collection to CAD model creation. For examples, in data acquisition phase, boundary information is useful for measurement region division and measurement path optimization. In data segmentation phase, boundary information is critical for data classification. In the next surface fitting phase, boundary information is helpful for fast feature recognition. And in the last CAD model generation phase, boundary information is essential for surface boundary reconstruction and accuracy evaluation for the final reconstructed result.

According to the different contributions to RE modeling, the boundary information can typically be classified into two types: 1) Modeling Support Boundary Information (MSBI) and 2) Modeling Used Boundary Information (MUBI), in which MSBI refers to the boundary data that is only used to assist, simplify or optimize the phases of RE modeling process, while MUBI refers to the boundary data that is directly used for CAD model reconstruction or accuracy evaluation. Therefore, compared with MUBI, the precision requirement of MSBI is much lower due to their different purposes to RE modeling.

Currently, there are many different methods for acquiring surface boundary information. The existing methods are mainly of two types: contact methods and non-contact methods. Contact methods generally measure the surface boundaries manually by using a mechanical touch probe that attached to an arm of a Coordinate Measuring Machine (CMM) such as guide tracked CMM, articulated arm CMM or optical CMM, etc[2-3]. Non-contact methods usually employ optical sensors to obtain boundary information. One extensively used method is stereo image detection, in which vision sensors (CCD/COMS cameras) are adopted to capture boundary information based on binocular stereo vision or multi-view stereo vision[4-8]. Another commonly used non-contact method is optical 3D scanning, in which stripe and area typed 3D optical sensors such as laser line scanners or structured lighting sensors are used to scan the measured surface intensively, then intelligent feature recognition algorithms are applied to extract the surface boundaries from the scanning data obtained by the optical sensors[9-12]. Comparatively, contact methods have higher accuracy, repeatability and reliability but much lower efficiency. Besides, the boundary information acquired by contact methods is tend to be influenced by human factors due to the limitation of manual control measurement. Stereo image detection as a type of non-contact method has the advantages of simple measurement principle, low cost sensors and fast measurement speed. But the accuracy of measurement result is limited, moreover, the critical issue of image matching has not yet fully solved. The surface boundary information generated from optical scanning data has medium accuracy, but it is acquired in the data segmentation phase which means no boundary information can be available for measurement planning in the data acquisition phase when using this method.

Taking the requirement of precision level, measurement speed and cost into consideration, stereo vision is a reasonable choice for acquiring MSBI. Image matching (corresponding points matching, stereo matching, stereo correspondence), which is the matching of the same physical points in two different images, is the key problem of stereo-vision-based 3D measurement, and it is also one of the most active research spot in the field of computer vision[13-15] At present, the existing algorithms for image matching mainly fall into two categories: area-based (gray value- based) matching[16-18], feature-based matching[19-21]. The prominent difference between them is the matching

primitives they choose for image representation. The area-based methods choose the gray values of subset areas which is typically square windows centered at the candidate matching points as the matching primitives, while feature-based methods choose the features of the interest points. The area-based algorithms have relatively simple matching principle, however it tends to be influenced by image distortion such as affine distortion or radiation distortion, and it is also sensitive to the illumination, contrast and noise of the images. Moreover, it is difficult to determine the sizes and shapes of the subset areas which directly affect matching accuracy. The feature-based matching algorithms such as Scale-Invariant Feature Transform (SIFT) matching algorithm[22-23], provides a set of accurate matching points, however, feature-based matching cannot provide sufficient information for dense matching and full-field matching. Recently, many area-feature or multi-cue fusion based matching approaches have been proposed to take advantages of different types of matching techniques[24-25].

Nevertheless, those mentioned matching algorithms are usually computational costly, and also may be leads to matching errors. Therefore, those matching algorithms are generally not used alone, but in combination with the epipolar geometric constraints between the two image planes. With the help of epipolar geometric constraints the search scope of the corresponding point can be narrowed from the whole image plane down to a straight line, by which the amount of computation can be greatly reduced and the matching accuracy can also be improved. However, there is no special geometric relationships between the two epipolar lines such as parallel or intersect at a fixed angle in common binocular stereo vision. Therefore, the calculation of epipolar lines is usually complicated and matching errors may still present in the final matching result.

In order to acquire the MSBI both rapidly and easily, the Coaxial Stereo Vision Photogrammetry (CSVP) is explored in depth[26-28], and then a new approach for digitizing surface boundary based on CSVP is proposed. In this method, the characteristics of the CSVP epipolar geometry, in which the epipolar lines in the two image planes are arranged parallel to each other, and these two epipolar lines pass through the main points of their own image planes respectively, were applied to facilitate image matching. A CMM was employed as the measurement platform to build the CSVP measurement system. Based on the capability of the CMM for precise spatial positioning, only one camera was used to carry out CSVP. Experimental results indicate that the MSBI can be obtained both rapidly and easily by CSVP, and the precision level of the measurement result can meet the accuracy requirements of MSBI in reverse engineering.

1 Measurement principle of CSVP

The measurement principle of CSVP is shown in Fig. 1, where O_1 and O_2 are the optical center of the front camera C_{Front} and the back camera C_{Back} respectively, F and B denote the image planes of C_{Front} and C_{Back}, O_{F} and O_{B} are the main points (the intersection points between the optical axis and the image plane) of F and B. As shown in Fig. 1, C_{Front} and C_{Back} are located coaxially, which means the optical axis of two cameras coincide with each other. Therefore, O_1, O_{F}, O_2 and O_{B} are on a straight line, and $F /\!/ B$. $O_{\text{F}}X_{\text{F}}Y_{\text{F}}$ and $O_{\text{B}}X_{\text{B}}Y_{\text{B}}$ which taking O_{F} and O_{B}as their origins are the image coordinate systems of F and B, and $oxyz$with the origin at O_1 is the common reference coordinate system of the two cameras. Let $P(x,y,z)$ be a measured point in the working volume, then the corresponding image points of P on the image planes F and B are denoted as $P_{\text{F}}(X_{\text{F}},Y_{\text{F}})$ and $P_{\text{B}}(X_{\text{B}},Y_{\text{B}})$ respectively. $Q(x,\ z)$ is the orthographic projection point of P on the plane xoz, and the corresponding mage points of Q on F and B are denoted by $Q_{\text{F}}(X_{\text{F}},0)$ and $Q_{\text{B}}(X_{\text{B}},0)$. In Fig. 1, $O_2E /\!/ ox$, and the projected point of Q on ox and O_2E are labeled as G_{F} and G_{B}. Assume that the focal length of the cameras C_{Front} and C_{Back} are f_{F} and f_{B} , then $|\ O_1\ O_{\text{F}}\ | = f_{\text{F}}$, and $|\ O_2\ O_{\text{B}}\ | = f_{\text{B}}$. The baseline distance of the two cameras which is the distance between O_1 and O_2 is defined as L, that is $|\ O_1O_2\ | = L$.

As shown in Fig. 1, by similar triangles which is $\Delta QO_1G_{\text{F}} \backsim \Delta O_1Q_{\text{F}}O_{\text{F}}$, we have

$$\frac{|\ O_1G_{\text{F}}\ |}{|\ Q_{\text{F}}O_{\text{F}}\ |} = \frac{|\ QO_1\ |}{|\ O_1Q_{\text{F}}\ |} = \frac{|\ QG_{\text{F}}\ |}{|\ O_1O_{\text{F}}\ |} \tag{1}$$

By $\Delta O_1PQ \backsim \Delta O_1P_{\text{F}}Q_{\text{F}}$, we have

$$\frac{|\ PQ\ |}{|\ P_{\text{F}}Q_{\text{F}}\ |} = \frac{|\ QO_1\ |}{|\ Q_{\text{F}}O_1\ |} \tag{2}$$

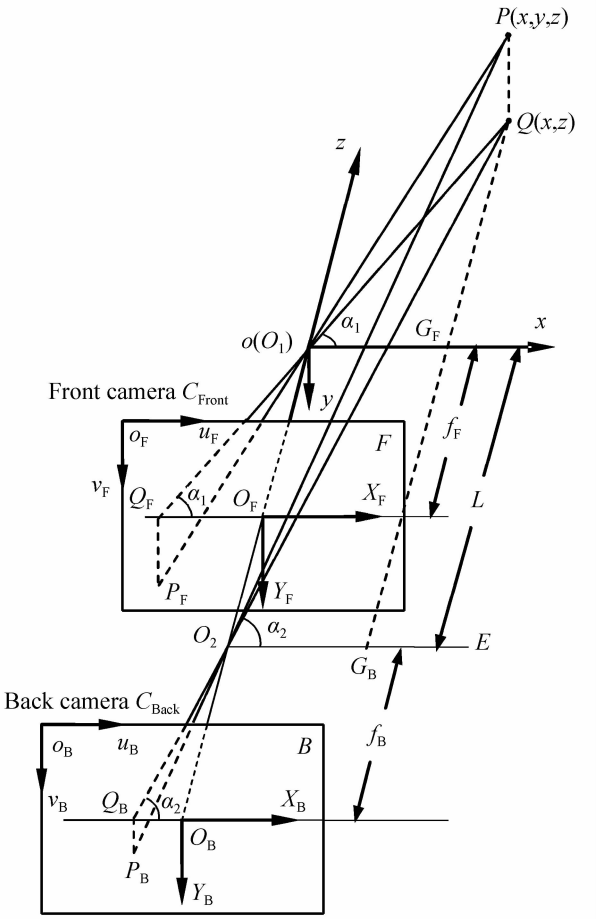

Fig. 1 Measurement principle of CSVP

Combining Eq. (1) and (2) gives

$$\frac{|O_1G_F|}{|Q_FO_F|}=\frac{|PQ|}{|P_FQ_F|}=\frac{|QG_F|}{|O_1O_F|} \tag{3}$$

which can be expressed in the form

$$-\frac{x}{X_N}=-\frac{y}{Y_N}=\frac{z}{f_N} \tag{4}$$

Similarly, by $\Delta QO_2G_B\backsim\Delta O_2Q_BO_B$, we have

$$\frac{|O_2G_B|}{|Q_BO_B|}=\frac{|QO_2|}{|O_2Q_B|}=\frac{|QG_B|}{|O_2O_B|} \tag{5}$$

By $\Delta PQO_2\backsim\Delta P_BQ_BO_2$, we have

$$\frac{|PQ|}{|P_BQ_B|}=\frac{|QO_2|}{|Q_BO_2|} \tag{6}$$

Combining Eqs. (5) and (6) gives

$$\frac{|O_2G_B|}{|Q_BO_B|}=\frac{|PQ|}{|P_BQ_B|}=\frac{|QG_B|}{|O_2O_B|} \tag{7}$$

which can also be expressed in the form

$$-\frac{x}{X_F}=-\frac{y}{Y_F}=\frac{z+L}{f_F} \tag{8}$$

Combining Eqs. (4) and (8) gives

$$\begin{cases}x=LX_FX_B/(X_Bf_F-X_Ff_B)\\ y=LX_BY_F/(X_Bf_F-X_Ff_B)\\ z=LX_Bf_F/(X_Ff_B-X_Bf_F)\end{cases} \tag{9}$$

or

$$\begin{cases} x = LX_F Y_B / (Y_B f_F - Y_F f_B) \\ y = LY_F Y_B / (Y_B f_F - Y_F f_B) \\ z = LY_B f_F / (Y_F f_B - Y_B f_F) \end{cases} \tag{10}$$

where X_F, Y_F and X_B, Y_B are the coordinates in $O_F X_F Y_F$ and $O_B X_B Y_B$ respectively.

Both $O_F X_F Y_F$ and $O_B X_B Y_B$ are the coordinate systems expressed in length such as in millimeter, but for actual images, the positional or distance parameters are more commonly expressed in pixels. Therefore, as shown in Fig. 1, another two pixel based image coordinate systems $o_F u_F v_F$ and $o_B u_B v_B$ with the origins at o_F and o_B are established for the image panels F and B. Assume that the pixel coordinate of O_F in $o_F u_F v_F$ is (u_{0F}, v_{0F}), and the pixel coordinate of O_B in $o_B u_B v_B$ is (u_{0B}, v_{0B}), then the coordinate transformation relationships between $o_F u_F v_F$ and $O_F X_F Y_F$, $o_B u_B v_B$ and $O_B X_B Y_B$ can be derived as follows

$$\begin{cases} X_F = (u_F - u_{0F}) d_X \\ Y_F = (v_F - v_{0F}) d_Y \\ X_B = (u_B - u_{0B}) d_X \\ Y_B = (v_B - v_{0B}) d_Y \end{cases} \tag{11}$$

where d_X and d_Y are the physical sizes of a single pixel in the horizontal and vertical direction respectively.

Substituting Eq. (11) into Eqs. (9) and (10) results in

$$\begin{cases} x = \dfrac{L(u_F - u_{0F})(u_B - u_{0B})}{[(u_B - u_{0B})\alpha_{xF} - (u_F - u_{0F})\alpha_{xB}]} \\ y = \dfrac{L(u_B - u_{0B})(v_F - v_{0F})}{[(u_B - u_{0B})\alpha_{yF} - (u_F - u_{0F})\alpha_{yB}]} \\ z = \dfrac{L(u_B - u_{0B})\alpha_{xF}}{[(u_F - u_{0F})\alpha_{xB} - (u_B - u_{0B})\alpha_{xF}]} \end{cases} \tag{12}$$

or

$$\begin{cases} x = \dfrac{L(u_F - u_{0F})(v_B - v_{0B})}{[(v_B - v_{0B})\alpha_{xF} - (v_F - v_{0F})\alpha_{xB}]} \\ y = \dfrac{L(v_F - v_{0F})(v_B - v_{0B})}{[(v_B - v_{0B})\alpha_{yF} - (v_F - v_{0F})\alpha_{yB}]} \\ z = \dfrac{L(v_B - v_{0B})\alpha_{yF}}{[(v_F - v_{0F})\alpha_{yB} - (v_B - v_{0B})\alpha_{yF}]} \end{cases} \tag{13}$$

where α_{xF}, α_{yF} and α_{xB}, α_{yB} are the scale factors (effective focal length) of u and v axis on the front and back image plane. And $\alpha_{xF} = f_F / d_X$, $\alpha_{yF} = f_F / d_Y$, $\alpha_{xB} = f_B / d_X$ and $\alpha_{yB} = f_B / d_Y$.

According to the Eq. (12) or Eq. (13), it can be seen that if the baseline distance is determined, then the 3D coordinates of the measured point can be calculated by the 2D pixel coordinates of its image points in the two cameras.

2 Measurement accuracy analysis of CSVP

Currently, little work has been done on measurement accuracy analysis of CSVP. The Refs. [26] and [28] analysed the effect of system parameters on the measurement accuracy of CSVP, however, some of the analysis results are necessary to further discussion. According to Eq. (9), it can be easily observed that the parameters which influence the CSVP measurement result include the baseline distance L, the focal lengths f_F, f_F and the coordinates (X_F, Y_F), (X_B, Y_B) of the image points on the F and B. The effects of these parameter on CSVP measurement accuracy will be discussed below based on Eq. (9).

According to Eq. (9), the partial derivatives of x with respect to X_F and X_B can be written as

$$\begin{cases} \dfrac{\partial x}{\partial X_F} = \dfrac{L X_B^2 f_F}{(X_B f_F - X_F f_B)^2} \\ \dfrac{\partial x}{\partial X_B} = -\dfrac{L X_F^2 f_B}{(X_B f_F - X_F f_B)^2} \end{cases} \tag{14}$$

The equivalent of Eq. (14) can be expressed as

$$\begin{cases} \dfrac{\partial x}{\partial X_F} = \dfrac{1}{L f_F} \cdot \left(\dfrac{L X_B f_F}{X_B f_F - X_F f_B} \right)^2 \\ \dfrac{\partial x}{\partial X_B} = -\dfrac{(L X_B f_F / (X_F f_B - X_B f_F) + L)^2}{L f_B} \end{cases} \tag{15}$$

From Eq. (9), we have

$$LX_{\mathrm{B}}f_{\mathrm{F}}/(X_{\mathrm{F}}f_{\mathrm{B}}-X_{\mathrm{B}}f_{\mathrm{F}})=z \tag{16}$$

Substituting Eq. (16) into Eq. (15) results in

$$\begin{cases}\dfrac{\partial x}{\partial X_{\mathrm{F}}}=\dfrac{z^2}{Lf_{\mathrm{F}}}\\ \dfrac{\partial x}{\partial X_{\mathrm{B}}}=-\dfrac{(z+L)^2}{Lf_{\mathrm{B}}}\end{cases} \tag{17}$$

According to Eq. (9), the partial derivatives of x with respect to Y_{F} and Y_{B} can be expressed as

$$\begin{cases}\partial x/\partial Y_{\mathrm{F}}=0\\ \partial x/\partial Y_{\mathrm{B}}=0\end{cases} \tag{18}$$

According to Eq. (9), the partial derivatives of y with respect to X_{F} and X_{B} can be calculated as

$$\begin{cases}\dfrac{\partial y}{\partial X_{\mathrm{F}}}=\dfrac{LX_{\mathrm{B}}Y_{\mathrm{F}}f_{\mathrm{B}}}{(X_{\mathrm{F}}f_{\mathrm{B}}-X_{\mathrm{B}}f_{\mathrm{F}})^2}\\ \dfrac{\partial y}{\partial X_{\mathrm{B}}}=-\dfrac{LX_{\mathrm{F}}Y_{\mathrm{F}}f_{\mathrm{B}}}{(X_{\mathrm{B}}f_{\mathrm{F}}-X_{\mathrm{F}}f_{\mathrm{B}})^2}\end{cases} \tag{19}$$

rewriting Eq. (19) gives

$$\begin{cases}\dfrac{\partial y}{\partial X_{\mathrm{F}}}=-\dfrac{LX_{\mathrm{B}}Y_{\mathrm{F}}}{X_{\mathrm{B}}f_{\mathrm{F}}-X_{\mathrm{F}}f_{\mathrm{B}}}\cdot\dfrac{LX_{\mathrm{B}}f_{\mathrm{F}}}{X_{\mathrm{F}}f_{\mathrm{B}}-X_{\mathrm{B}}f_{\mathrm{F}}}\cdot\dfrac{f_{\mathrm{B}}}{X_{\mathrm{B}}}\cdot\dfrac{1}{Lf_{\mathrm{F}}}\\ \dfrac{\partial y}{\partial X_{\mathrm{B}}}=\dfrac{LX_{\mathrm{B}}Y_{\mathrm{F}}}{X_{\mathrm{B}}f_{\mathrm{F}}-X_{\mathrm{F}}f_{\mathrm{B}}}\cdot\left(\dfrac{LX_{\mathrm{B}}f_{\mathrm{F}}}{X_{\mathrm{F}}f_{\mathrm{B}}-X_{\mathrm{B}}f_{\mathrm{F}}}+L\right)\cdot\dfrac{1}{Lf_{\mathrm{B}}}\cdot\dfrac{f_{\mathrm{B}}}{X_{\mathrm{B}}}\end{cases} \tag{20}$$

From Eq. (9), we can obtain

$$LX_{\mathrm{B}}Y_{\mathrm{F}}/(X_{\mathrm{B}}f_{\mathrm{F}}-X_{\mathrm{F}}f_{\mathrm{B}})=y \tag{21}$$

by $\Delta O_2Q_{\mathrm{B}}O_{\mathrm{B}}\backsim\Delta QO_2G_{\mathrm{B}}$, we have

$$f_{\mathrm{B}}/X_{\mathrm{B}}=-(z+L)/x \tag{22}$$

Substituting Eqs. (16), (21), (22) into Eq. (20) results in

$$\begin{cases}\dfrac{\partial y}{\partial X_{\mathrm{F}}}=\dfrac{yz(z+L)}{xLf_{\mathrm{F}}}\\ \dfrac{\partial y}{\partial X_{\mathrm{B}}}=-\dfrac{y(z+L)^2}{xLf_{\mathrm{B}}}\end{cases} \tag{23}$$

Then, according to Eq. (9), the partial derivatives of y with respect to Y_{F} and Y_{B} can be expressed as

$$\begin{cases}\dfrac{\partial y}{\partial Y_{\mathrm{F}}}=\dfrac{LX_{\mathrm{B}}}{X_{\mathrm{B}}f_{\mathrm{F}}-X_{\mathrm{F}}f_{\mathrm{B}}}=-\dfrac{LX_{\mathrm{B}}f_{\mathrm{F}}}{f_{\mathrm{F}}(X_{\mathrm{F}}f_{\mathrm{B}}-X_{\mathrm{B}}f_{\mathrm{F}})}\\ \dfrac{\partial y}{\partial Y_{\mathrm{B}}}=0\end{cases} \tag{24}$$

Substituting Eq. (16) into Eq. (24) results in

$$\begin{cases}\dfrac{\partial y}{\partial Y_{\mathrm{F}}}=-\dfrac{z}{f_{\mathrm{F}}}\\ \dfrac{\partial y}{\partial Y_{\mathrm{B}}}=0\end{cases} \tag{25}$$

Next, according to Eq. (9), the partial derivatives of z with respect to X_{F} and X_{B} can be written as

$$\begin{cases}\dfrac{\partial z}{\partial X_{\mathrm{F}}}=-\dfrac{LX_{\mathrm{B}}f_{\mathrm{F}}f_{\mathrm{B}}}{(X_{\mathrm{F}}f_{\mathrm{B}}-X_{\mathrm{B}}f_{\mathrm{F}})^2}\\ \dfrac{\partial z}{\partial X_{\mathrm{B}}}=\dfrac{LX_{\mathrm{F}}f_{\mathrm{F}}f_{\mathrm{B}}}{(X_{\mathrm{F}}f_{\mathrm{B}}-X_{\mathrm{B}}f_{\mathrm{F}})^2}\end{cases} \tag{26}$$

The equivalent of Eq. (26) can be expressed as

$$\begin{cases}\dfrac{\partial z}{\partial X_{\mathrm{F}}}=-\dfrac{(LX_{\mathrm{B}}f_{\mathrm{F}})^2}{(X_{\mathrm{F}}f_{\mathrm{B}}-X_{\mathrm{B}}f_{\mathrm{F}})^2}\cdot\dfrac{1}{Lf_{\mathrm{F}}}\cdot\dfrac{f_{\mathrm{B}}}{X_{\mathrm{B}}}\\ \dfrac{\partial z}{\partial X_{\mathrm{B}}}=\dfrac{1}{Lf_{\mathrm{B}}}\cdot\left[\left(\dfrac{LX_{\mathrm{B}}f_{\mathrm{F}}}{X_{\mathrm{F}}f_{\mathrm{B}}-X_{\mathrm{B}}f_{\mathrm{F}}}\right)^2+\dfrac{L^2X_{\mathrm{B}}f_{\mathrm{F}}}{X_{\mathrm{F}}f_{\mathrm{B}}-X_{\mathrm{B}}f_{\mathrm{F}}}\right]\cdot\dfrac{f_{\mathrm{B}}}{X_{\mathrm{B}}}\end{cases} \tag{27}$$

Substituting Eqs. (16) and (22) into Eq. (27) results in

$$\begin{cases}\dfrac{\partial z}{\partial X_{\mathrm{F}}}=\dfrac{z^2(z+L)}{xLf_{\mathrm{F}}}\\ \dfrac{\partial z}{\partial X_{\mathrm{B}}}=-\dfrac{z(z+L)^2}{xLf_{\mathrm{B}}}\end{cases}\tag{28}$$

Finally, according to Eq. (9), the partial derivatives of z with respect to Y_{F} and Y_{B} can be expressed as

$$\begin{cases}\partial z/\partial Y_{\mathrm{F}}=0\\ \partial z/\partial Y_{\mathrm{B}}=0\end{cases}\tag{29}$$

Assume that the measurement uncertainties of the front and back cameras are δX_{F}, δX_{B} in X direction and δY_{F}, δY_{B} in Y direction respectively. Let Δx, Δy, Δz be the measurement error separations of the measured point P in x, y, z directions respectively, then Δx can be calculated as

$$\Delta x=\left|\frac{\partial x}{\partial X_{\mathrm{F}}}\right|\delta X_{\mathrm{F}}+\left|\frac{\partial x}{\partial X_{\mathrm{B}}}\right|\delta X_{\mathrm{B}}+\left|\frac{\partial x}{\partial Y_{\mathrm{F}}}\right|\delta Y_{\mathrm{F}}+\left|\frac{\partial x}{\partial Y_{\mathrm{B}}}\right|\delta Y_{\mathrm{B}}\tag{30}$$

substituting Eqs. (17) and (18) into Eq. (30) results in

$$\Delta x=\frac{z^2}{Lf_{\mathrm{F}}}\delta X_{\mathrm{F}}+\frac{(z+L)^2}{Lf_{\mathrm{B}}}\delta X_{\mathrm{B}}\tag{31}$$

Δy can be expressed as

$$\Delta y=\left|\frac{\partial y}{\partial X_{\mathrm{F}}}\right|\delta X_{\mathrm{F}}+\left|\frac{\partial y}{\partial X_{\mathrm{B}}}\right|\delta X_{\mathrm{B}}+\left|\frac{\partial y}{\partial Y_{\mathrm{F}}}\right|\delta Y_{\mathrm{F}}+\left|\frac{\partial y}{\partial Y_{\mathrm{B}}}\right|\delta Y_{\mathrm{B}}\tag{32}$$

substituting Eqs. (23) and (25) into Eq. (32) results in

$$\Delta y=\left|\frac{y}{x}\right|\cdot\frac{z(z+L)}{Lf_{\mathrm{F}}}\delta X_{\mathrm{F}}+\left|\frac{y}{x}\right|\cdot\frac{(z+L)^2}{Lf_{\mathrm{B}}}\delta X_{\mathrm{B}}+\frac{z}{f_{\mathrm{F}}}\delta Y_{\mathrm{F}}\tag{33}$$

Δz can be written as

$$\Delta z=\left|\frac{\partial z}{\partial X_{\mathrm{F}}}\right|\delta X_{\mathrm{F}}+\left|\frac{\partial z}{\partial X_{\mathrm{B}}}\right|\delta X_{\mathrm{B}}+\left|\frac{\partial z}{\partial Y_{\mathrm{F}}}\right|\delta Y_{\mathrm{F}}+\left|\frac{\partial z}{\partial Y_{\mathrm{B}}}\right|\delta Y_{\mathrm{B}}\tag{34}$$

substituting Eqs. (28) and (29) into Eq. (34) results in

$$\Delta z=\frac{z^2(z+L)}{|x|Lf_{\mathrm{F}}}\delta X_{\mathrm{F}}+\frac{z(z+L)^2}{|x|Lf_{\mathrm{B}}}\delta X_{\mathrm{B}}\tag{35}$$

To simplify the complexity of calculation, we may take $\delta X_{\mathrm{F}}=\delta X_{\mathrm{B}}=\delta Y_{\mathrm{F}}=\delta Y_{\mathrm{B}}=\delta$ and $f_{\mathrm{F}}=f_{\mathrm{B}}=f$. Then the Eqs. (31), (33) and (35) can be rewritten as follows

$$\begin{cases}\Delta x=\dfrac{2z^2+2zL+L^2}{Lf}\delta\\ \Delta y=\dfrac{|y/x|(2z^2+3zL+L^2)+zL}{Lf}\delta\\ \Delta z=\dfrac{1}{|x|}\cdot\dfrac{(2z^3+3z^2L+zL^2)}{Lf}\delta\end{cases}\tag{36}$$

upon rearrangement, gives

$$\begin{cases}\Delta x=\dfrac{\delta z}{f}\left(2\dfrac{z}{L}+\dfrac{L}{z}+2\right)\\ \Delta y=\dfrac{\delta z}{f}\left[\left|\dfrac{y}{x}\right|\left(2\dfrac{z}{L}+\dfrac{L}{z}+3\right)+1\right]\\ \Delta z=\dfrac{\delta z}{f}\cdot\dfrac{z}{|x|}\left(2\dfrac{z}{L}+\dfrac{L}{z}+3\right)\end{cases}\tag{37}$$

Let Δxyz be the composed error at the measuring position P, then Δxyz can be calculated as

$$\Delta xyz=\sqrt{(\Delta x)^2+(\Delta y)^2+(\Delta z)^2}\tag{38}$$

substituting Eq. (37) into Eq. (38) results in

$$\Delta xyz=\frac{\delta z}{f}\sqrt{(M+2)^2+\left[\left|\frac{y}{x}\right|(M+3)+1\right]^2+\frac{z^2}{x^2}(M+3)^2}\tag{39}$$

where $M=2\dfrac{z}{L}+\dfrac{L}{z}$.

According to Eq. (39), the following three categories can be concluded:

1) When the focal length of two cameras f_{F} and f_{B} increase, the composed measurement error Δxyz will decrease which means the measurement accuracy of CSVP will be improved. Therefore, the usage of

long telephoto lens in CSVP can obtain relatively high measurement accuracy.

2) When the position of the measured point gets closer to the common optical axis of two cameras, $|x|$ will decrease, while the value of Δxyz will get larger which means the measurement accuracy of CSVP will be reduced. If the measured point is located on the optical axis, then $|x|=0$ which leads to Δxyz approaching infinity. Therefore, the CSVP is not capable of measuring the points on the optical axis in space.

3) The baseline distance L exist both in the numerator and denominator in Eq. (39), which result in nonlinear influence on the measurement accuracy.

The influence of baseline distance on the measurement accuracy can be analysed by Eq. (39). It can be easily observe from Eq. (39) that if the coordinates of the measured point $P(x, y, z)$ are determined, then M is the only factor affecting the value of Δxyz.

From Eq. (39), we have

$$M=2\frac{z}{L}+\frac{L}{z}\geqslant\sqrt{2\frac{z}{L}\cdot\frac{L}{z}}=\sqrt{2} \tag{40}$$

Hence, $M_{\min}=\sqrt{2}$ if and only if $2\frac{z}{L}=\frac{L}{z}$, that is $L=\sqrt{2}z$. It indicates that Δxyz has the minimum at $L=\sqrt{2}z$.

Substituting $M_{\min}=\sqrt{2}$ into Eq. (39) results in

$$\Delta xyz_{\min}=\frac{\delta z}{f}\sqrt{(\sqrt{2}+2)^2+\left[\left|\frac{y}{x}\right|(\sqrt{2}+3)+1\right]^2+\frac{z^2}{x^2}(\sqrt{2}+3)^2} \tag{41}$$

Let $\frac{L}{z}=k$, then according to Eq. (39) we have $M=k+\frac{2}{k}$. The graph of $M(k)$ is given in Fig. 2, from Fig. 2 it can be observed that if $k\in(1,2)$, the change of k causes little impact on the value of M. If $k<1$, the change of k has a great influence on the value of M, and if k approaches to 0, the value of M increases sharply and tends to $+\infty$. If $k>2$, then M almost increases linearly (the slope is about 1) with the increasing of k.

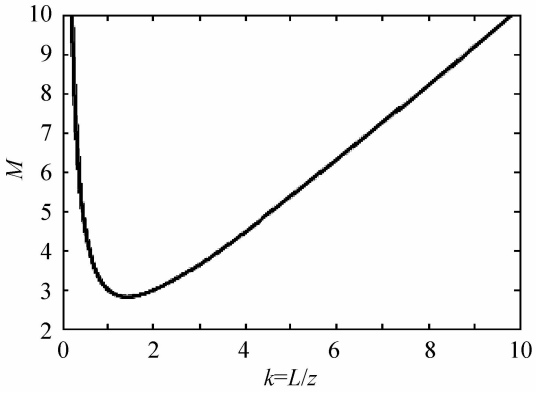

Fig. 2 Effect of baseline distance on measurement accuracy

Based on the analysis above, it can be concluded that the baseline distance L should be set in a neighbourhood of $L=1.4z$ when applying CSVP, it should be avoid to set the value of L at the region where $L<z$.

3 Epipolar geometry of CSVP

The simplified geometrical model of CSVP is illustrated in Fig. 3, where O_1 and O_2 are the optical centers of the C_{Front} and the C_{Back} respectively, F and B are the image planes of C_{Front} and C_{Back}, O_F and O_B are the main points of F and B. Let $P(x,y,z)$ an arbitrary measured point, and its corresponding image points on the planes F and B are P_F and P_B respectively. According to the epipolar geometry of stereo vision O_1O_2 which joining the optical centres is the baseline of the measurement model, and the intersections of O_1O_2 and F, B are the epipoles of the two image planes[29]. Here, the epipoles of the two image

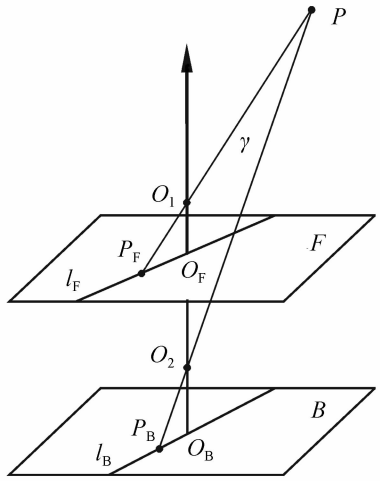

Fig. 3 Epipolar geometry of CSVP

planes coincide with their corresponding main points O_F, O_B since the two cameras are arranged coaxially. The plane γ which is defined by P, O_1 and O_2 is the epolar plane of the measurement model. The lines l_F and l_B which are the intersecting lines of γ and the two image planes are the epipolar lines of F and B respectively. On the basis of the epipolar geometry of stereo vision, all the epipolar lines intersect at the epipoles of their own image planes[29]. In CSVP we have $l_F \parallel l_B$ due to$F \parallel B$, and all the epipolar lines on the F pass through O_F, on the B pass through O_B since the epipoles of image planes and their main points O_F, O_B coincide.

From the analysis results above, the characteristics of CSVP epipolar geometry can be concluded as follow:1) The two epipolar lines, which corresponding to the same measured point, on the front and back image planes are arranged parallel to each other. 2) All the epipolar lines on the image planes pass through the main points of their own image planes respectively.

The epipolar constraint in stereo vision is that given a point in the reference image, then its corresponding point in the target image is constrained to lie on the epiploar line of the given point. By epipolar constraint the search space for correspondences can be reduced from the whole image to a line which is very beneficial for image matching. In conventional stereo vision system, the essential matrix or the fundamental matrix should be determined first for calculating the epiploar line of the given point, which is complex and also a research spot in the field of stereo vision.

In CSVP, taking the above mentioned characteristics of epipolar geometry into consideration, the computation of epiploar line can be significantly simplified. As shown in Fig. 3, suppose P_F is the image point of P on F, then the corresponding epiploar line of P_F on B can be obtained in the following two steps: 1) connect P_F and O_1, and denote P_FO_F as l_F; 2) Draw a line l_B which passes through O_B and is parallel with l_F. Then l_B is the epiploar line of P_F on B. Then the corresponding point of P_F on l_B can be determined based on image intensity, image feature or other criterions.

4 Implementation of CSVP

4.1 CSVP based on two cameras

According to the measurement principle of CSVP as shown in Fig. 1, the two cameras should be arranged as that shown in Fig. 4, where the C_{Front} is positioned directly in front of the C_{Back}. However, following Fig. 4, it is obviously that the view field of C_{Back} will be obstructed by C_{Front}. Therefore, it is unreasonable to employ this configuration for CSVP application.

The structure in Fig. 4 can be improved to solve the blocking problem by a beam-splitter as shown in Fig. 5. In this method, the two cameras are positioned in such a way that the optical axes of the two cameras are perpendicular to each other and intersect at the point O, a beam-splitter is placed at O in such a way that the angles between the beam splitter and two optical axes are both 45°. According to Fig. 5, the light reflected from the measured object can be separated into two perpendicular beams (the reflected beam

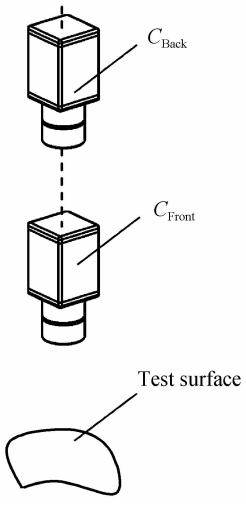

Fig. 4 Theoretical position of the two cameras

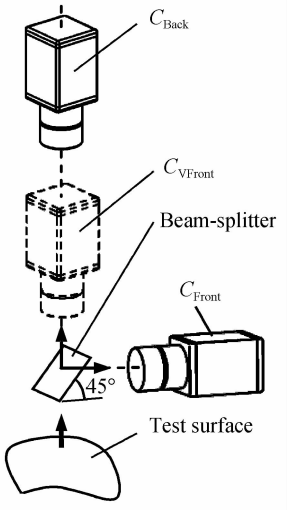

Fig. 5 CSVP based on beam splitter

and transmitted beam) by the beam-splitter. Then the reflected beam enters into C_{Front} while the transmitted beam into C_{Back}. With this method the C_{Front} is able to provide images the same as that captured by the virtual front camera C_{VFront} which is positioned directly in front of the C_{Back}. Therefore, the architecture in Fig. 5 is applicable for CSVP.

4.2 Single camera CSVP based on CMM

Although the proposed method in Fig. 5 is effective for CSVP, the realization of this measurement system requires two cameras, and it is difficult to meet the positioning requirement of the components in the conceptual system in Fig. 5. Therefore, taking a CMM as the platform, a novel one camera CSVP is proposed. As shown in Fig. 6, the camera is mounted onto the Z-arm of a CMM. Single camera CSVP includes two steps below: 1) the camera is moved to the front image-capturing position by the CMM, and then takes an image of the test object as the front image; 2) The camera is moved a baseline distance along Z-axis with X and Y axes fixed by the CMM, and then takes another image of the test object as the back image.

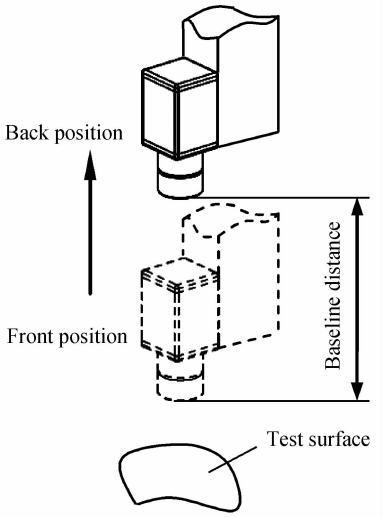

Fig. 6 Single camera CSVP based on CMM

Due to the precision mechanical structure , the CMM is capable of accurate positioning. Therefore, based on the CMM, the coaxality of the two cameras and the precise baseline distance between the two measuring position can be effectively guaranteed. In addition, this measurement method utilizes only one camera, by which the sensor cost can be reduced and the consistency of camera parameters at the two measurement position can be assured. Therefore, following the two step above, CSVP can be implemented effectively.

According to the single camera CSVP mentioned above, the basic premise of applying this method is to have a CMM which is a widely used standing machine in the field of geometric measurement. If a CMM is not available, it may be not appropriate to adopt this method, since it would be too expensive to implement it.

5 Surface boundary digitization based on CSVP

Although the characteristics of epipolar geometry in CSVP can simplify the image matching process, its disadvantage, which is the measurement accuracy will sharply decrease if the measured point get close to the optical axis of two cameras, makes it not suitable for digitizing surfaces. But when the camera's optical axis aligns with the center of the measured surface, the surface boundaries generally locate at the periphery of the image. Therefore, CSVP can be applied for acquiring the boundary information of the measured surface, from which the characteristics of CSVP epipolar geometry can be taken advantage of but the disadvantages of CSVP can be avoided.

5.1 Edge extraction in image

After obtaining the image pairs of the measured surface by the approach of single camera CSVP as mentioned above, the edges in images should be extracted first for acquiring 3D boundary information. Here Steger, which is the commonly used algorithm for edge detecting in image processing, is employed to extract the edges in the images. Before measurement, the measured surface may need to be sprayed a layer of white developer to help the boundaries to be mapped to the images clearly . Taking the pictures of a mouse

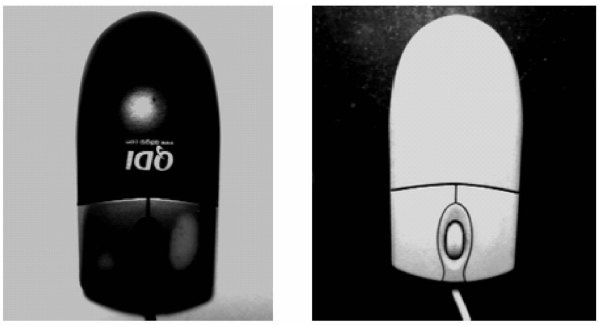

(a) Before using developer (b) After using developer

Fig. 7 Effect of developer on boundary identification in images

as an example, the effect of developer on sharpness of the contours in the images is shown in Fig. 7, where Fig. 7(a) shows the image of the mouse without using developer while Fig. 7(b) did. It is apparent that the contours of mouse surface is much more distinguishable in Fig. 7(b).

5.2 Image matching in CSVP

From the measurement principle of CSVP, it can be easily obtained that the field of view of C_{Front} is smaller than that of C_{Back}, which means that the scene in the front image must be contained in the back image. Therefore, the front image should be chosen as the reference image when performing image matching task. Otherwise, a number of points in the reference image may be unmatchable.

As shown in Fig. 8, suppose that Fig. 8(a) and Fig. 8(b) are the edge extraction results of an image pair, in which P_{F} is captured by C_{Front} and P_{B} by C_{Back}, O_{F} and O_{B} are the main points of P_{F} and P_{B}, $O_{\text{F}}X_{\text{F}}Y_{\text{F}}$ and $O_{\text{B}}X_{\text{B}}Y_{\text{B}}$ are the image coordinate system of P_{F} and P_{B} respectively. Then the matching procedure involves the following three steps.

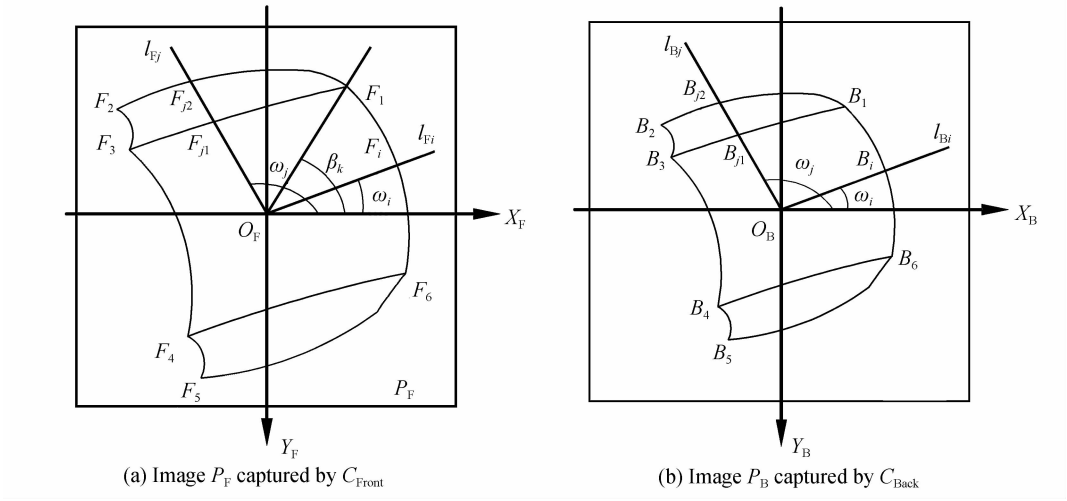

Fig. 8 Image matching process of CSVP

5.2.1 Corner matching. In Fig. 8, it is possibly that corner points exist in edge features. Corner points are the segment points of edge features, and they are crucial for boundary reconstruction. Therefore, corner matching should be performed first in the image matching process. In Fig. 8(a), Harris algorithm is employed to detect the corners on the edge features in P_{F}[30-31], and six corners which denoted asF_k ($1\leqslant k\leqslant 6$) are extracted. Similarly, as shown in Fig. 8(b), another six corners that denoted by B_t ($1\leqslant t\leqslant 6$) can be obtained in P_{B}. Then F_k and B_t are sorted following the same rule. The sorting rule is as follows: firstly, the angles between $O_{\text{F}}F_k$ and $O_{\text{F}}X_{\text{F}}$ which are denoted as β_k are calculated, then F_k ($1\leqslant k\leqslant 6$) are sorted in ascending order according to the value of β_k. Similarly, the sorted sequence of B_t ($1\leqslant t\leqslant 6$) can be acquired. Finally, F_k and B_t are matched in order of k and t, that is

$$F_k \leftrightarrow B_t \quad (1\leqslant k=t\leqslant 6) \tag{42}$$

If the edge features in images are complex, then the number of the detected corners in P_{F} may be different from that in P_{B}. Then further selections need to be made based on the values of the corresponding inclination angles of the corners. Furthermore, additional constraints such as the distance between the corners and the main point of the image plane for sorting may be needed.

5.2.2 Image matching based on epipolar constraint. Apart from corners, other points on the edges will be matched on the basis of epipolar constraint. According to the characteristics of CSVP epipolar geometry, O_{F} and O_{B} in Fig. 8 are the two epipoles of P_{F} and P_{B} respectively. Taking P_{F} as the reference image, the matching procedure is as follows: 1) In P_{F}, draw a sampling ray l_{Fi}, starting at O_{F}, and intersects the edge features at F_i, then a sampling angle ω_i is generated as shown in Fig. 8(a); 2) By the characteristics of CSVP epipolar geometry, the matching point of F_i in P_{B} must be on the epipolar, which passes through the epipole O_{B} on P_{B} and is parallel to l_{Fi}, that corresponding to F_i. Therefore, draw a sampling ray l_{Bi} starting at O_{B} on P_{B} in such a way that the angle between l_{Bi} and $O_{\text{B}}X_{\text{B}}$ is equal to ω_i and intersects the edge features in P_{B} at B_i as shown in Fig. 8(b). Obviously, $l_{Fi} \parallel l_{Bi}$, hence B_i is the corresponding point of F_i; 3) Given $\Delta\omega$ as the cyclic increment, repeat step 1～3 until $\omega_i \geqslant 2\pi$ is reached.

5.2.3 Image matching based on consistency of arrangement. In practical application, it is possibly that the sampling ray has more than one intersections with the edge features, which may lead to matching errors only based on epipolar constraint. Therefore, additional constraint should be taken into consideration to guarantee the uniqueness of stereo matching. Consistency of arrangement in image matching means the corresponding matching points are arranged in the same order on their respective epipolars[29]. Let l_{Fj} be one sampling ray which makes a sampling angle of ω_j with $O_F X_F$ and intersects with the edge features at F_{j1} and F_{j2} as in Fig. 8(a). By epipolar constraint we can get the matching points B_{j1} and B_{j2} in Fig. 8(b). Then further matching based on arrangement consistency is performed as follows: 1) Calculate the distance between each candidate matching point and the origin of their image plane; 2) Sort F_{j1} and F_{j2}, B_{j1} and B_{j2} respectively in ascending order according to the distances obtained in step1; 3) Match in order. In Fig. 8, the final matching result is as follows: $F_{j1} \leftrightarrow B_{j1}$, $F_{j2} \leftrightarrow B_{j2}$. The same method can be applied in corner matching when two corners are distributed on the same sampling ray.

After image matching, the 3D coordinates of the measured points can be obtained by substituting the matched point pairs into Eq. (9) or Eq. (10).

If the distribution of the boundaries of the measured surface is complex, such as the edges are interlaced each other on the surface, then the measurement result may not come up to the requirements. Just as the curved surface S shown in Fig. 9(a), there exit edges that almost coincide with the sampling rays l, which may lead to false matching. Besides, according to the analysis in section 3, the measurement accuracy decreases as the measured point gets close to the optical axis of the camera. Therefore, the edges nearby the origin O in Fig. 9(a) may can't be measured precisely.

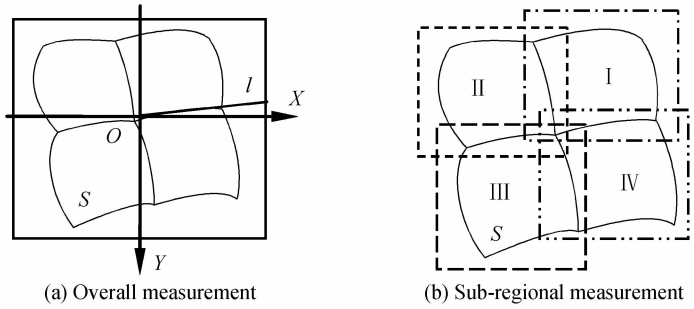

(a) Overall measurement (b) Sub-regional measurement

Fig. 9 Sub-regional measurement of surface boundaries

To improve the measurement accuracy, the measured surface can be divided into several sub-areas following the distribution features of the boundaries. As shown in Fig. 9(b), the whole surface S is divided into four sub-areas, then each sub-area is measured separately to obtain the sub-boundary-features. Finally, the overall boundary information can be acquired by combining the four sub-boundary-features.

5.3 Boundary reconstruction

5.3.1 Sampling point grouping. The measurement result of CSVP only provides the 3D coordinates of the sampling points, and no more information is available to illustrate dependency relations between the edges and the sampling points. Therefore, the obtained sampling points should be divided into groups first so that points belonging to the same curve segment are in the same group.

Fig. 10 shows the simulation measurement result of surface S as in Fig. 9, it can be observed from Fig. 10 that the boundary of S is divided into several curve segments by the corners. The strategy of sampling points grouping is as the following six steps.

1) As shown in Fig. 11(b), firstly define two arrays labeled as $\boldsymbol{C}$ and $\boldsymbol{P}$, then corners C_k ($1 \leqslant k \leqslant n$) are stored in the array $\boldsymbol{C}$. Both the boundary sampling points P_i ($1 \leqslant i \leqslant m$) and the corners C_k ($2 \leqslant k \leqslant n$) are stored in the array $\boldsymbol{P}$.

2) Define a new array labeled as $\boldsymbol{R}_1$, and put the first element of $\boldsymbol{C}$ which is C_1 into $\boldsymbol{R}_1$. Then taking C_1 as the reference point, calculate the distances between C_1 and each element of $\boldsymbol{P}$ to find the element which has the minimum distance. As shown in Fig. 11(a), assume that the final found element is P_i (suppose $|C_1 P_i| = d_0$), then$P_i$will be stored in $\boldsymbol{R}_1$, and be deleted from $\boldsymbol{P}$.

3) As shown in Fig. 11(a), take P_i as the new reference point in $\boldsymbol{R}_1$, then search its nearest point in $\boldsymbol{P}$ by distance calculation. Assume that the nearest point of $P_i$is P_{i+1} as in Fig. 11(a), then the value of

$\angle C_1P_iP_{i+1}$ will be calculated, if $\angle C_1P_iP_{i+1}<120°$, where 120° is defined by experience, then P_{i+1} is considered as a pseudo-homogeneous point. Then the task of searching for the nearest point of P_i in $\boldsymbol{P}$ except P_{i+1} will continue until the required point is found. Here, we suppose $\angle C_1P_iP_{i+1}>120°$, then P_{i+1} will be stored in $\boldsymbol{R}_1$ and be deleted from $\boldsymbol{P}$.

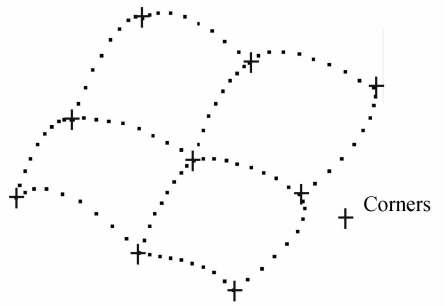

Fig. 10 Simulative boundary measurement result of S

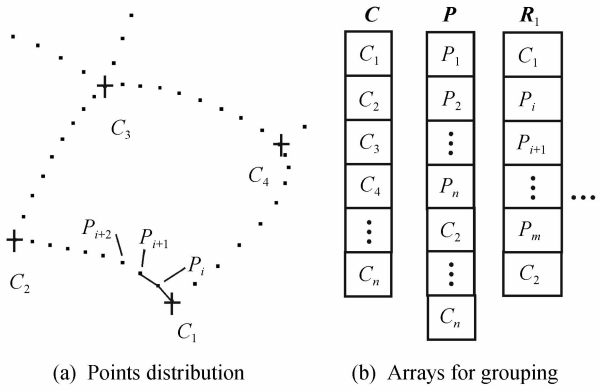

Fig. 11 Sampling points classification process

4) Repeat step 3 until the searching result of step 3 is a corner point such as C_2, then C_2 will be stored in $\boldsymbol{R}_1$ so that the points in $\boldsymbol{R}_1$ represents a curve segment of the surface boundaries.

5) Still take C_1 as the reference point, cycle step 3 ~ 4 until the distance between C_1 and its nearest point is more than $10d_0$ (determined by experience). Then C_1 will be deleted from $\boldsymbol{C}$ and C_2 will be taken as the new reference point.

6) Repeat step 3 ~ 5 until no element is left in $\boldsymbol{C}$. As shown in Fig. 10, twelve arrays denoted as $\boldsymbol{R}_t$ ($1\leqslant t\leqslant 12$), in which ordered data points representing twelve segments of boundaries are stored, can be obtained after grouping.

5.3.2 Boundary reconstruction. The main task of boundary reconstruction is to reconstruct each boundary segment with B-spline curves based on the grouped data points. There are mainly two methods to construct B-spline curves if the data points is given, that is interpolation and fitting. Comparatively, the curves generated by fitting method generally have better smoothness. In practical application, B-spline curves with 2 to 4 orders are widely used for curve fitting. Therefore, fitting method with cubic spline functions are employed here to reconstruct the surface boundary segments. Today, there are many commercial 3D modeling softwares available for B-spline curves construction, such as CATIA, NX, ProE, SolidWorks, etc. Fig. 12 shows the boundary reconstruction result of the data points in Fig. 10 by Siemens NX software, in which the allowable error is set as 0.01mm, and cubic B-spline curves is adopt to fit the boundary segments.

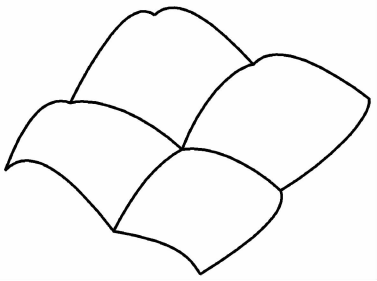

Fig. 12 Simulative boundary reconstruction result of S

6 Experimental verification

The experimental setup for demonstrating the feasibility of CSVP is shown in Fig. 13. Fig. 13(a) shows the BQC654 CMM, which was taken as the measurement platform in this experiment. Fig. 13(b) shows the JAI CV-A50 camera which was the key sensor in this experiment. The physical pixel size of the camera is $d_X\times d_Y=8.6\times 8.3$ μm, and the physical resolution is 752×582. The camera was equipped with a Computar M0814-M lens with a focal length of 8mm. Fig. 13(c) shows the Renishaw touch probe. The touch probe has high level of measurement accuracy (3~5 μm within 3σ) compared to vision sensors, therefore, the measurement result of touch probe was considered as the truth value for measurement accuracy evaluation.

(a) CMM (b) Camera and lens (c) Touch probe

Fig. 13 CMM and sensors for experiment

As shown in Fig. 14(a), a fruit plate made of polymethyl methacrylate was served as a test object, and it was denoted by S_P. White developer was sprayed on the surface of S_P to improve image contrast. The experiment was carried out as follow:

1) Sensor Installation. The camera was mounted on the Z arm of the CMM, and a ring-shaped LED light was equipped in front of the camera lens to ensure good illumination.

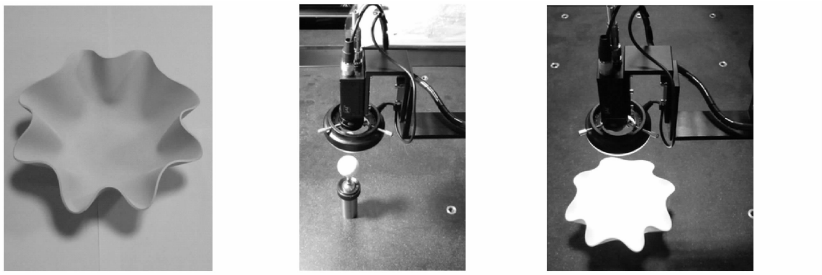

(a) Test object S_P (b) Determine reference (c) Measuring S_P

Fig. 14 Boundary measurement process by CVSP

2) Camera parameter calibration. The parameters needed to be calibrated includes α_x, α_y, u_0 and v_0 (their definitions see section 2), here the parameter of nonlinear distortion and the factor of pixel non-verticality were not taken into consideration, since the camera lens applied in this experiment was not wide-angle lens, the distortion is very small and it can be ignored. In addition, most of the commercial available CCD cameras have a good pixel verticality nowadays, and they have minor effect on the experimental results. In this experiment, the planar conic based method was applied to calibrate the camera parameters[3], the calibration results is listed in Table 1.

Table 1 Internal parameters calibration results of the camera

α_x	α_y	u_0/pixel	v_0/pixel
914.53	947.59	378.15	288.72

3) Measurement coordinate system establishment. As shown in Fig. 14(b), a reference ball was placed on the platform of the CMM, the measurement coordinate system was established with the origin at the center of the reference ball.

4) Image acquisition at the front position. As shown in Fig. 14(c), the Z arm of the CMM was adjusted such that the camera was aligned with S_P and clear images could be acquired. After that the distance between the lens and S_P was measured by a simple ruler, it was about 0.25 m, then the baseline distance was determined by $L=1.4\times0.24=0.35$ m. Finally, the image of S_P at the front position was captured as in Fig. 15(a) and denoted by M_F.

5) Image acquisition at the back end. The Z arm of the CMM was lifted by a baseline distance that was 0.35 m with the X and Y axes fixed. Then the image of S_P at the back end was captured as in Fig. 15(b) and denoted by M_B.

6) Edge extraction. The Steger algorithm was applied to extract the edge features in M_F and M_B, the results are shown in Fig. 15(c) and Fig. 15(d).

7) Image matching. The M_F was taken as the reference image, and the method illustrated in section 5.2 was employed to perform image matching task.

8) 3D coordinates acquisition. The pairs of the matched points and the calibrated parameters were substituted into Eq. (12) or Eq. (13) to acquire the 3D coordinates of the sampling points on edge features, the calculation result is given in Fig. 15(e).

9) Boundary fitting. The 3D sampling points acquired by step 8 were fitted with B-spline curves using the method described in section 5.3, and the final fitted boundary of the test object is given in Fig. 15(f).

10) Reference points acquisition. The touch probe that fitted with a styli with sharp tip was mounted onto the Z arm of the CMM, and the reference ball was measured firstly to determine the location of the touch probe with respect to the measurement coordinate system, then the boundaries of S_P was measured by the touch probe manually. The acquired reference points is shown in Fig. 15(g).

11) Deviation analysis. The deviations between the reference points and the fitted surface boundaries were calculated by Siemens NX software to evaluate the feasibility of CSVP. The analysis results is shown in Table 2.

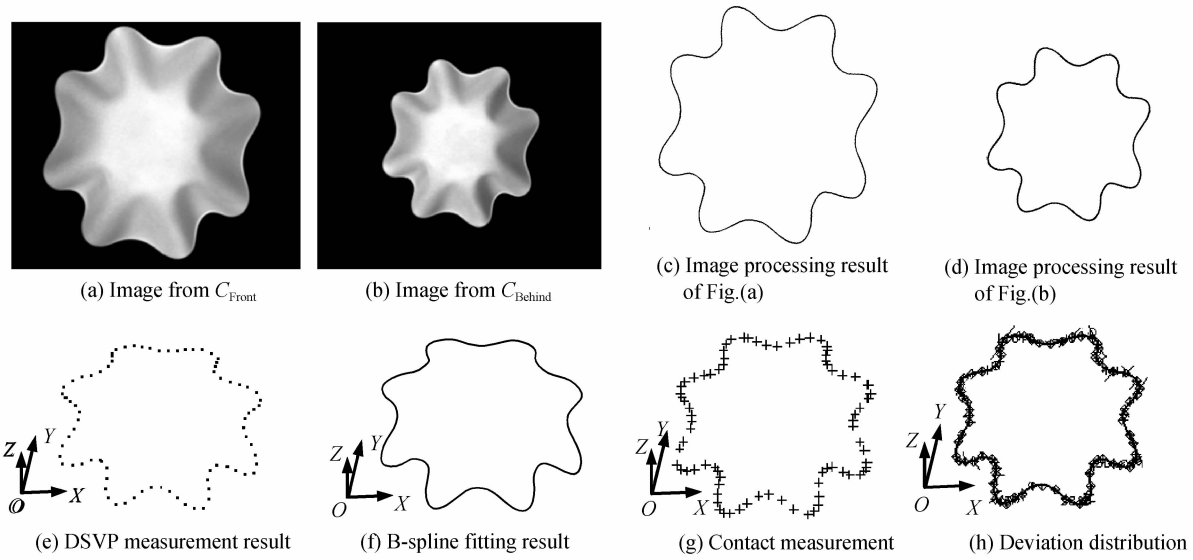

Fig. 15 Data processing of CSVP for curve boundary measurement

Table 2 Deviation analysis of CSVP measurement result

Figure of Measurement result	Figure of reference points	Maximum deviation ε_{max}/mm	Average deviation $\bar{\varepsilon}$/mm
15(f)	15(g)	0.576	0.268

According to Table 2, it can be learned that measurement accuracy of the CSVP is not as good as commercial stereo vision sensor. The reasons cause measurement errors may include as follows: 1) Limitation of the measuring principle of CSVP (see the measurement accuracy analysis in section 2); 2) Due to the different shooting distance, the magnification of the same object in the two matching images is obviously different (see Fig. 15(a) and (b)), this difference may reduce the stereo matching accuracy. 3) An existed camera parameter calibration method was applied, no research was carried out to establish a calibration method specifically for CSVP, and some of the camera parameters were ignored for simplifying the calibration process; 4) The commonly used Steger algorithm was employed for edge features extraction, and no more further pixel subdivision was performed.

Nevertheless, here the boundary information acquired by CSVP is just for supporting the RE modeling process, such as for measurement area division, measurement planning for digitizer, guiding the subsequent data processing, etc. And the measurement result of CSVP would not be applied for geometric modeling, therefore the measurement result basically meets the accuracy requirements of MSBI in reverse engineering.

Besides, compared with the common stereo vision photogrammetry, the stereo matching process of CSVP is much simpler. Therefore, the stereo matching algorithm of CSVP would be much more easily realized which helps it easy to be integrated into other systems such as CMM measurement systems.

In addition, if the boundary features needed to be measured are located in the holes or on the inner

concave surfaces, then CSVP may be more advantageous, as in CSVP the two cameras are arranged on the same line, therefore the two cameras are in the same angle of view by which the influence of the barrier by the hole wall on the camera's view field will be much smaller than that of common stereo vision.

7 Conclusion

1) CSVP is applicable for 3D measurement; the usage of long telephoto lens in CSVP can obtain relatively high measurement accuracy; the measurement accuracy of CSVP will be reduced if the position of the measured point gets closer to the common optical axis of the two cameras, and the CSVP is not capable of measuring the points on the optical axis in space.

2) The influence of baseline distance on the measurement accuracy is nonlinear; and the baseline distance L should be set in a neighbourhood of $L=1.4z$ (z represents the distance between the camera lens and the measured object) when perform CSVP, it should be avoid to set the value of L at the region where $L<z$.

3) In CSVP, the two corresponding epipolar lines on the front and back image planes are arranged parallel to each other, and they pass through the main points of their own image planes respectively. By making use of this special epipolar geometry in CSVP, the image matching process can be simplified remarkably.

4) The experiment results indicate that CSVP can be implemented using a single camera by taking advantage of the CMM's capability of accurate positioning; the average error of the surface boundaries reconstructed by the data gathered by the proposed method is 0.268mm. It can meet the accuracy requirements of modeling support boundary information in reverse engineering.

References

[1] RAJA V, FERNANDES K J. Reverse engineering: an industrial perspective[M]. London:Springer, 2008.

[2] XIE Z X,WANG J W,ZHANG Q M. Complete 3D measurement in reverse engineering using a multi-probe system[J]. *International Journal of Machine Tools and Manufacture*, 2005, **45**(12-13): 1474-1486.

[3] LI F, LONGSTAFF A P, FLETCHER S. Rapid and accurate reverse engineering of geometry based on a multi-sensor system[J]. *International Journal of Advanced Manufacturing Technology*, 2014, **74**(1-4): 369-382.

[4] LU Bao-li, LIU Yu-liang, SUN Liang. Error analysis of binocular stereo vision system applied in small scale measurement[J]. *Acta Photonica Sinica*, 2015, **44**(10): 1011001

[5] XIANG H Y, HAN B A, HUANG J J. Surface reconstruction of stamping parts based on binocular stereo vision[J]. *Applied Mechanics and Materials*, 2013, **415**: 314-17.

[6] XU W F, DENG L, ZHENG Q. Using stereo vision to construct 3-D surface models[J]. *IEEE Potentials*, 2012, **31**(2): 31-37.

[7] LIU Hao-ran, ZHANG Wen-ming, LIU Bin. Three dimension measurement based on the binocular vision[J]. *Acta Photonica Sinica*, 2009, **38**(7): 1830-1834.

[8] HE Bing-wei, LIN Zhi-hang. Extracting boundary curve of complex surface using trinocular stereo vision[J]. *Journal of Computer-aided Design & Computer Graphics*, 2003, **15**(10): 1253-1257.

[9] PINTO T, KOHLER C, ALBERTAZZI A. Regular mesh measurement of large free form surfaces using stereo vision and fringe projection[J]. *Optical and Lasers in Engineering*, 2012, **50**(7): 910-916.

[10] ZHU H, CONG L. A feature-based section curve reconstructing strategy[J]. *Key Engineering Materials*, 2014, **572**: 155-158.

[11] LI Hai-lun, LI Rong, DING Guo-fu, *et al*. Genetic fuzzy clustering algorithm for point cloud data segmentation[J]. *Application Research of Computers*, 2012, **29**(5): 1974-1979.

[12] LIU Ning, LU Rong-sheng, XIA Rui-xue, *et al*. A novel algorithm for computing the plane of line structured light in 3D vision measurement[J]. *Acta Photonica Sinica*, 2012, **41**(2): 179-184.

[13] LIU K, ZHOU C, WEI S, *et al*. Optimized stereo matching in binocular three-dimensional measurement system using structured light[J]. *Applied Optics*, 2014, **53**(26): 6083-6090.

[14] ZHANG H, ZHAO L, WANG L. A new binocular vision stereo matching algorithm[J]. *Applied Mechanics and Materials*, 2013, **389**: 721-725.

[15] WANG Yu, CHEN Dian-ren, PIAO Yan, *et al*. Improved viewing quality of reconstructed three-dimensional image based on texture features of matching regions[J]. *Acta Photonica Sinica*, 2009, **38**(10): 2717-2721.

[16] HACHAJ T, OGIELA M R. Real time area-based stereo matching algorithm for multimedia video devices[J]. *Opto-electronics Review*, 2013, **21**(4): 367-375.

[17] SHIMIZU M, OKUTOMI M. Multi-parameter simultaneous estimation on area-based matching[J]. *International*

Journal of Computer Vision, 2006, **67**(3): 327-342.

[18] SHIMIZU M, OKUTOMI M. Sub-pixel estimation error cancellation on area-based matching[J]. *International Journal of Computer Vision*, 2005, **63**(3): 207-224.

[19] TAN X, SUN C M, SIRAULT X, *et al*. Feature matching in stereo images encouraging uniform spatial distribution [J]. *Pattern Recognition*, 2015, **48**(8): 2530-2542.

[20] KIM T J, SEO Y H, KIM D W, *et al*. A feature-based and hierarchical stereo matching method[J]. *International Journal of Innovative Computing Information and Control*, 2011, **7**(12): 6785-6797.

[21] JAZAYERI I, FRASER C S. Interest operators for feature-based matching in close range photogrammetry [J]. *Photogrammetric Record*, 2010, **25**(129): 24-41.

[22] JOGLEKAR J, GEDAM S S, MOHAN B K. Image matching using SIFT features and relaxation labeling technique- a constraint initializing method for dense stereo matching[J]. *IEEE Transactions on Geoscience and Remote Sensing*, 2014, **52**(9): 5643-5652.

[23] SUN Y B, ZHAO L, HUANG S D, *et al*. L^2-SIFT feature extraction and matching for large images in large-scale aerial photogrammetry[J]. *ISPRS Journal of Photogrammetry and Remote Sensing*, 2014, **91**: 1-16.

[24] QIU M J, ZHANG Y. Feature guided multi-window area-based matching method for urban remote sensing stereo pairs [C]. IGARSS, 2015, 4510-4513.

[25] JOGLEKAR J, GEDAM S S, MOHAN B K. Image matching using SIFT features and relaxation labeling technique - a constraint initializing method for dense stereo matching[J]. *IEEE Transactions on Geoscience and Remote Sensing*, 2014, **52**(9): 5643-5652.

[26] XIONG Lan-hui, WANG Yuan-qing. Depth measurement by co-axial stereo vision[J]. *Modern Electronics Technique*. 2012, **35**(6): 115-122.

[27] KONG Min, WANG Shi-min. The research of 3D measurement based on coaxial stereo vision[J]. *Acta Metrologica Sinica*, 2004, **25**(4): 294-297.

[28] LIU Bai-gao, YUAN Li-xing, ZHENG Nan-ning, *et al*. Several camera geometry models and error analysis for image matching in 3-D machine vision[J]. *Acta Photonica Sinica*, 1997, **26**(8): 737-741.

[29] ZHANG Guang-jun. Vision measurement[M]. Beijing: Science Press, 2008.

[30] CUI J, XIE J B, LIU T, *et al*. Corners detection on finger vein images using the improved Harris algorithm[J]. *International Journal for Light and Electron Optics*, 2014, **125**(17): 4668-4671.

[31] ZHANG Cong-peng, WEI Xue-guang. Rectangle detection based on Harris corner [J]. *Optics and Precision Engineering*, 2014, **22**(8): 2259-2266.

[32] YANG Chang-jiang, SUN Feng-mei, HU Zhan-yi. Planar conic based camera calibration[J]. *Chinese Journal of Computers*, 2000, **23**(5): 541-547.